Experimental and numerical study of shock-accelerated elliptic heavy gas cylinders

Jing-song Bai,[1] Li-yong Zou,[2] Tao Wang,[1] Kun Liu,[1] Wen-bin Huang,[2] Jin-hong Liu,[2] Ping Li,[1] Duo-wang Tan,[2] and Cang-li Liu[2]

[1]*Institute of Fluid Physics, China Academy of Engineering Physics, Mianyang, Sichuan, People's Republic of China*

[2]*National Key Laboratory of Shock Wave and Detonation Physics (LSD), Institute of Fluid Physics, China Academy of Engineering Physics, Mianyang, Sichuan, People's Republic of China*

(Received 1 July 2010; published 16 November 2010)

We studied the evolution of elliptic heavy SF_6 gas cylinder surrounded by air when accelerated by a planar Mach 1.25 shock. A multiple dynamics imaging technology has been used to obtain one image of the experimental initial conditions and five images of the time evolution of elliptic cylinder. We compared the width and height of the circular and two kinds of elliptic gas cylinders and analyzed the vortex strength of the elliptic ones. Simulations are in very good agreement with the experiments, but due to the different initial gas cylinder shapes, a certain difference of the initial density peak and distribution exists between the circular and elliptic gas cylinders, and the latter initial state is more sensitive and more inenarrable.

DOI: 10.1103/PhysRevE.82.056318 PACS number(s): 47.40.Nm, 47.20.Ma

An instability induced by a shock wave colliding with an interface between two materials of different density is known as the Richtmyer-Meshkov (RM) instability. Numerous papers [1–4] have investigated the experimental techniques and simulation methods of the shock-accelerated circular heavy gas cylinder. As we all know, initial conditions have a major effect on the development and evolution of the interface instability throughout the process. A one-dimensional (1D) finite interfacial transition layer (ITL) or "diffused cylinder" has been posed by Gupta *et al.* [5]. ITL is an important consideration for the validity of the simulations at late time and an important aspect for comparison with experimental results. These kinds of hydrodynamic RM experiments are mainly realized in shock tubes [6–10]. Many scientists stress the uncertainty in the initial conditions of the interface and the resulting even more uncertainty in the use of experimental data to test numerical schemes. In all known horizontal or vertical shock tube experiments, the initial interfacial conditions are rarely accurately measured [11,12] but often backward estimated. Recently, the authors investigated the influence of nonuniform flow initial conditions on the interface instability [13] with well-conducted experiments and numerical simulations. Our work illuminated that besides owning the identity of initial interface condition, the initial nonuniform flow would have a significant effect on the RM instability.

This research is motivated by the interest of understanding and controlling the noncircular (elliptic in this paper) gas cylinder shock tube instability experiments and numerical simulations. We arranged three experiments to achieve this goal. The first one was a preparative experiment, in which a shock wave accelerated a circular gas cylinder, while in the two others, the elliptic heavy gas cylinders were driven by shocks in two different vertical directions. The objective of our work is to study the relationship between the circular and elliptic gas cylinders and construct approximate initial conditions of two-dimensional (2D) diffuse ITL with finite thickness to elliptic ones. In particular, we also analyzed the effect of convergence and vortex features of the induced gas cylinders with time under different shock-accelerated directions to the elliptic gas cylinder. This is another experimental and numerical study with a shock-accelerated elliptic heavy gas cylinder.

The experiments were performed in the National Key Laboratory of Shock Wave and Detonation Physics horizontal shock tube which is 5 m long and 5×5 cm^2 square cross section. It was coupled with a high-speed multiple dynamics imaging technology (the interval between two consecutive frames was 100 μs) which allows a 2D visualization of the interface. Tracer fog was applied to the gas to enhance the light scattered and charge-coupled device cameras were used to increase the dynamic range of the images. The interface between light gas (air) and heavy gas (SF_6) was created using a cylindrical contoured nozzle with a diameter of 5.0 mm for the circular gas cylinder, while in the elliptic cases, an elliptic cylindrical contoured nozzle with its major and minor axes of 10.0 mm and 2.5 mm, respectively, was adopted. The Mach number of the incident shock wave was 1.25 in air. Table I summarizes the properties of air and SF_6 gas in the present experiments at 0.97 atm and 20 °C. By using the multiple dynamics imaging technology, we obtained one image of the experimental initial conditions and five images of the time evolution of the cylinder two-dimensional diagram from $t=200$ to 600 μs at intervals of 100 μs. Figure 1 shows the typical frames obtained for the three experiments [Figs. 1(a), 1(c), and 1(e)] and simulations [Figs. 1(b), 1(d), and 1(f)].

The pressure of initial SF_6 gas cylinder is 0.97 atm and the initial spatial distribution of density is difficult to be measured and not known. In our experiments, we mainly estimated the SF_6 gas concentrations at the center of the gas cylinder from the initial images; they are approximate about of 0.87 and 0.71, respectively. Therefore, we need to determine the initial distribution of density in the gas cylinder with the help of numerical simulation and experimental results in order to reproduce the whole experimental process and understand the impacts of different cylinder shapes and different shock-accelerated directions on the development and evolution of cylinders. This work has an important significance on the setting of initial conditions for experimental study of interface instability, analysis of experimental phenomenon, and results.

TABLE I. Properties of air and SF_6 gas.

Gas	Density (kg/m^3)	Specific heat ratio	Kinematic viscosity (10^{-6} m^2/s)	Prandtl number	Diffusion coefficient in air (cm^2/s)
Air	1.15	1.40	15.7	0.71	0.204
SF_6	5.34	1.09	2.47	0.90	0.097

This paper applies our large eddy simulation code multiviscous flow and turbulent (MVFT) to numerically simulate the multiviscosity fluid and turbulence. MVFT is based on the parabolic method [14], the Vreman [15] subgrid eddy viscosity model, and it solves the Navier-Stokes equations,

$$\frac{\partial \bar{\rho}}{\partial t} + \frac{\partial \bar{\rho}\tilde{u}_j}{\partial x_j} = 0,$$

$$\frac{\partial \bar{\rho}\tilde{u}_i}{\partial t} + \frac{\partial \bar{\rho}\tilde{u}_j\tilde{u}_i}{\partial x_j} + \frac{\partial \bar{p}}{\partial x_i} = \frac{\partial(\bar{\sigma}_{ij} + \tau_{ij})}{\partial x_j},$$

$$\frac{\partial \bar{\rho}\bar{E}}{\partial t} + \frac{\partial(\bar{\rho}\tilde{u}_j\bar{E} + \bar{p}\tilde{u}_j)}{\partial x_j} = -\frac{\partial(\bar{q}_j + Q_j)}{\partial x_j} + \frac{\partial[\tilde{u}_i(\bar{\sigma}_{ij} + \tau_{ij})]}{\partial x_j},$$

$$\frac{\partial \bar{Y}^{(s)}}{\partial t} + \tilde{u}_j\frac{\partial \bar{Y}^{(s)}}{\partial x_j} = \frac{\partial}{\partial x_j}\left(\tilde{D}\frac{\partial \bar{Y}^{(s)}}{\partial x_j}\right), \quad s = 1,2,\ldots,N-1, \tag{1}$$

Where $\bar{\sigma}_{ij} = \mu_l[\partial\tilde{u}_i/\partial x_j + \partial\tilde{u}_j/\partial x_i - 2/3\,\delta_{ij}(\partial\tilde{u}_k/\partial x_k)]$ is the viscous stress tensor, $\tau_{ij} = \bar{\rho}(u_iu_j - \bar{u}_i\bar{u}_j)$ is the subgrid scale (SGS) stress tensor, $\bar{q}_j + Q_j$ is the energy flux of unit time and space, $\bar{q}_j = -\lambda_l\partial\bar{T}/\partial x_j$, $Q_j = -\lambda_t\partial\bar{T}/\partial x_j$, $\lambda_l = \mu_l c_p/p_{r,l}$, $\lambda_t = \mu_t c_p/p_{r,t}$, $\tilde{D} = \bar{D}_l + D_t$, and $S_{c,t} = \mu_t/D_t\bar{\rho}$. μ_l is the fluid viscosity, μ_t is the turbulent viscosity, $\bar{T}$ is the temperature, λ_l is the efficient heat-transfer coefficient, c_p is the specific heat of fluid, $p_{r,l}$ is the Prandtl number, $\bar{D}_l$ is the diffusion coefficient, and D_t is the turbulent diffusion coefficient. N is one of the kinds of fluids and $\bar{Y}^{(s)}$ is the volume fraction of the sth fluid and satisfies $\Sigma_1^N\bar{Y}^{(s)} = 1$. An operator splitting technique is used to decompose the physical problems into three subprocesses in MVFT, i.e., the computations of inviscid flux, viscous flux, and heat flux. For the inviscid flux, the three-dimensional problem can be simplified into three 1D problems by dimension-splitting technique. For each 1D problem, we apply two-step Lagrange-Remap algorithm to solve the equations. During one time step, the calculation can be divided into four steps: (i) the piecewise parabolic interpolation of physical quantities, (ii) solving Riemann problems approximately, (iii) marching of Lagrange equations, and (iv) remapping the physical quantities to stationary Euler meshes. More information about the flow equations, algorithms, numerical schemes, SGS turbulent model, etc., can be obtained in the author's literature [13,16].

For the initial density distribution of the circular SF_6 gas cylinder in the first preparative experiment, numerical simulation is used to approximately describe the interface dissipative transition layer, the same as literature [5]. In the dissipative transition layer, SF_6 gas density is calculated by 1D Gaussian function,

$$\rho(r) = \chi_0\rho_{SF_6}e^{-[(r-r_c)^2/\delta^2]}, \tag{2}$$

where $r^2 = x^2 + y^2$, $r_c = 0.9$ mm, and $\delta = 2.15$ mm. χ_0 is the concentration at the center, $\chi_0 = 0.87$ in the circular case. The initial density image and distribution are plotted in Fig. 2(a).

However, for the elliptic SF_6 gas cylinders, i.e., in the second and third experiments, the initial density distributions are more complex than in the circular case in the numerical simulations. How to determine the density distributions of elliptic SF_6 gas cylinder is the first to be considered before the calculations, as it may directly impact on cylinder instability evolution. According to the experimental initial image and the interfacial transition layer assumption, an approximate "diffused elliptic cylinder" initial condition of 2D diffuse interfacial transition layer with finite thickness is constructed. The SF_6 gas density is calculated by 2D Gaussian function,

$$\rho(\alpha_k,\beta_k) = \chi_0\rho_{SF_6}e^{-[(\alpha_k-\alpha_{\min})^2+(\beta_k-\beta_{\min})^2]/\delta^2}, \tag{3}$$

$$\frac{(x-x_0)^2}{\alpha_k^2} + \frac{(y-y_0)^2}{\beta_k^2} < 1, \quad k = 1,M, \tag{4}$$

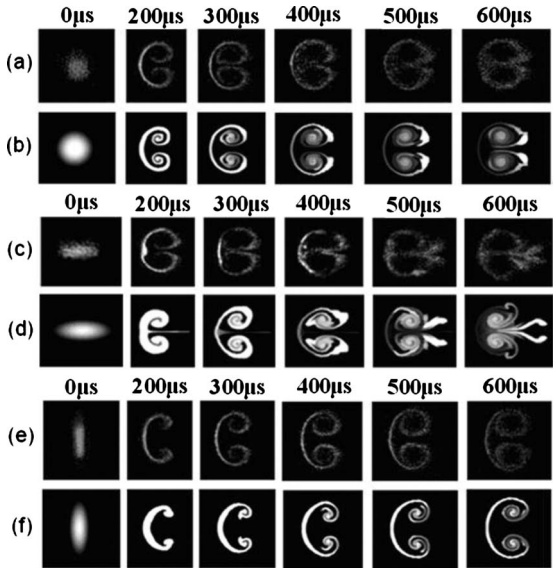

FIG. 1. Multiple dynamics images and numerical simulation results by MVFT at $t = 200$, 300, 400, 500, and 600 μs after shock passage. [The experiments corresponding (a), (c), and (e) and the simulations corresponding (b), (d), and (f).]

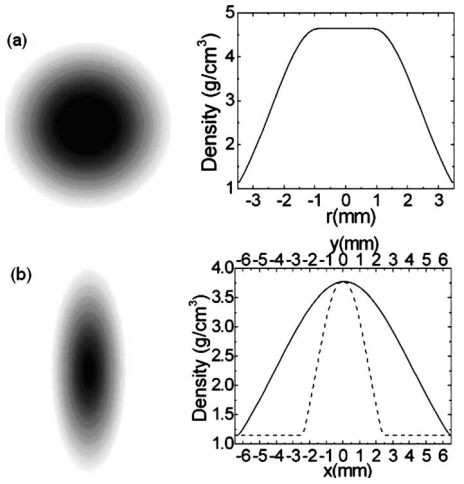

FIG. 2. The density images and distributions of the (a) circular and (b) elliptic SF_6 gas cylinder initially constructed. (The sizes of the images are same as Fig. 1.)

where $x_0=y_0=0$, $\alpha_k \in [\alpha_{\min}, \alpha_{\max}]$, $\beta_k \in [\beta_{\min}, \beta_{\max}]$, $\alpha_{\min}=\beta_{\min}=1.0\times 10^{-5}$ mm, $\alpha_{\max}=6.30$ mm, $\beta_{\max}=2.30$ mm, $\alpha_k=\alpha_{\min}+(k-1)d\alpha$, $\beta_k=\beta_{\min}+(k-1)d\beta$, $d\alpha=(\alpha_{\max}-\alpha_{\min})/M$, $d\beta=(\beta_{\max}-\beta_{\min})/M$, $M=1000$, and $\delta=6.16$ mm. χ_0 is the concentration at the elliptic center, $\chi_0=0.71$ in the elliptic case. The initial density image and distributions along major and minor axes of the ellipse are plotted in Fig. 2(b). The difference in the SF_6 gas concentrations at the center of the two kinds of gas cylinders leads to a certain difference in the initial density peaks and distributions between the circular and elliptic gas cylinders. In the circular case, a core with definite size radius could exist where the density is uniformly distributed. Although the idea of the elliptic initial density comes from the circular case, but under the cylindrical contoured nozzle with ellipse size of 2.5 mm$\times$10.0 mm and 2D diffuse effects, in our elliptic SF_6 gas cylinder experiment, not only the density peak is reduced but also the core may be absent in the symmetrical center of the cylinder.

Due to the symmetry of the gas cylinder and model, the calculating region $[-2.0\ \text{cm}, 18\ \text{cm}]\times[0.0\ \text{cm}, 2.5\ \text{cm}]$ is adopted, which is the upper half of the whole one $[-2.0\ \text{cm}, 18\ \text{cm}]\times[-2.5\ \text{cm}, 2.5\ \text{cm}]$, and it is discretized into 2500×312 grids. Sample images from the 2D numerical results are shown in Figs. 1(b), 1(d), and 1(f). These images have been chosen because they can illustrate some salient features of the experiments. From Figs. 1(a)–1(f), we can see that good qualitative agreement was achieved between the images obtained from the simulations and the experiments. Quantitative measurements allow us to perform a more rigorous comparison that can be made on the basis of a visual inspection of evolutionary images. In the three experiments, we mainly compared the length measurements of the evolving cylinders at each experimental time. The width and height of the evolving cylinders are measured using the six experimental and computational images. To distinguish the three experiments with three kinds of initial contoured nozzle, we use the shapes of these three kinds of initial contoured nozzles to denote them in our simulations. We define

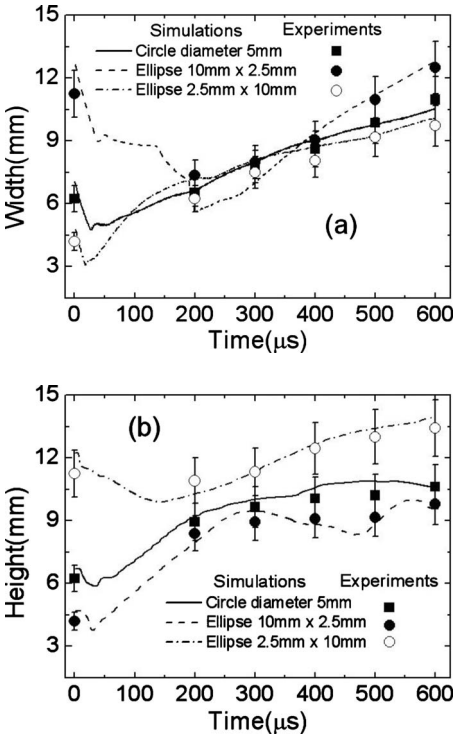

FIG. 3. Comparison of the width and height between the experiments and simulations. (The error bars of this visual measurement are equal to $\pm 10\%$.)

the width as the horizontal length or the streamwise dimension of the evolving cylinder and likewise the height as the vertical length or the spanwise dimension of the evolving cylinder, the same as in literature [17]. Plots of the width and height are shown in Fig. 3. We can see that quantitative agreements were achieved between the experimental and computational width and height of the evolving cylinders. Because of the errors in measuring the interface positions between air and diffused SF_6 gas from the experiment initial images, the initial width and height in our simulations are slightly greater than those in the experimental. Actually, the experimental and computational initial conditions were important for the width and height values, and the initial state of the elliptic is more sensitive and more inenarrable than the circular.

In the two vertical shock-accelerated directions to the elliptic heavy gas cylinder experiments, a large difference existed from the experiment images at the same times in Figs. 1(c) and 1(e) and the conclusion that the second experiment has stronger convergence than the third experiment was easily obtained. To illuminate this phenomenon from the simulations, we mainly analyze the vorticity, the circulation of each vortex, and the distance between the two vortex cores. In the MVFT code, vorticity is determined by calculating the curl of the velocity field. This relationship for the 2D flow is

$$\omega(x,y,t) = \nabla \times \mathbf{V} = \partial v/\partial x - \partial u/\partial y, \tag{5}$$

where $\mathbf{V}$ is the 2D velocity vector and u and v are the x and y components of the velocity. Circulation is a measure of the average vorticity over an area A,

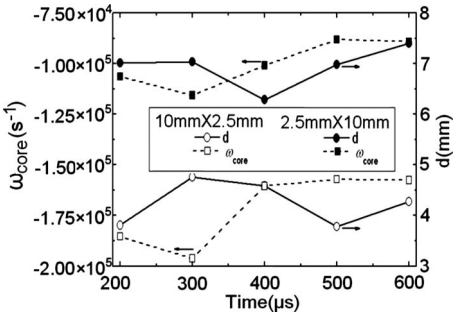

FIG. 4. The vorticity at the center of the core and the distance between the two vortex cores of these two simulations.

$$\Gamma(t) = \int_A \omega(x,y,t) \cdot dA. \tag{6}$$

In our experiments, the elliptic heavy gas cylinder evolves into a vortex pair due to the deposition of vorticity on the cylinder interface, and two obvious vortex cores are formed in the flow field. The vorticity has a negative maximum value in the vortex core of the upper half region we concerned and it has a positive maximum value in the vortex core of the lower half region. Here, we use a parameter d to describe the distance between the two vortex cores. Figure 4 shows the vorticity at the center of the core and the distance between the two vortex cores of these two simulations. We can see the evident difference between the two cases: the initial contoured nozzle of 10.0×2.5 mm^2 model has larger absolute values of $|\omega_{core}|$ at the center of the vortex cores than the 2.5×10.0 mm^2 model at the same time, with an average discrepancy factor of about 1.72 during the time 600 μs; the former has smaller d's than the latter, with an average discrepancy factor of about 0.61. Because of this, it appears that the 10.0×2.5 mm^2 model has a stronger effect of convergence than the 2.5×10.0 mm^2 model. In our calculation, the gas jet appears at the symmetry center of cylinder during the early times, shown in Fig. 1(d). This difference was due to the shockwave loading elliptic heavy gas cylinder in different major axis directions. Moreover, the results of verification can also be calculated by circulation. Figure 5 shows the positive circulation, the negative circulation, and the total circulation evolution over time of the flow field. From Fig. 5, it is clear that although the two models differ little in the positive circulation, the difference is more obvious in the negative circulation, resulting in the great difference in the total circulation of the flow field. The absolute

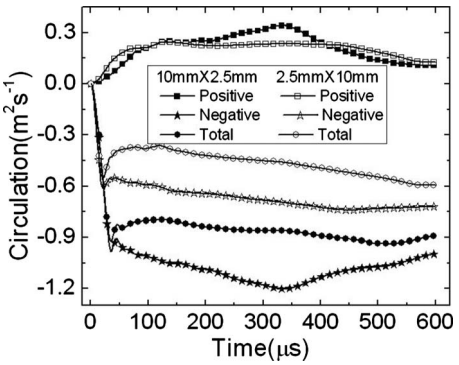

FIG. 5. The positive circulation, the negative circulation, and the total circulation evolution over time of the flow field of the two elliptic gas cylinders.

value of the former is larger than the latter, consistent with the results of the vorticity of the vortex cores. This phenomenon reveals features that previously studied circular cylinders do not have.

In summary, based on the circular gas cylinder experiment and simulations, we studied the evolution of elliptic heavy SF_6 gas cylinders surrounded by air when accelerated by planar shocks. The relationship between the elliptic and circular gas cylinders is constructed by an approximate initial condition of 2D diffuse ITL with finite thickness. By using a multiple dynamics imaging technology, the experiment initial conditions and five images of the time evolution of circular and elliptic cylinders were obtained. With the help of our numerical simulation tool, we compared the width and height of the circular and two kinds of elliptic gas cylinders and analyzed the effect of convergence and vortex features of the induced gas cylinder with time under the different shock-accelerated direction to the elliptic gas cylinder. However, due to the different initial gas cylinder shapes, a certain difference of the initial density peak and distribution existed between the circular and elliptic gas cylinder. In this investigation, although we succeeded in building a possible link between the gas columns, the elliptic ones are more complicated and hard to describe objective reality. Actually, it is difficult to be imagined for the more complex initial gas cylinder shapes.

The work was supported by the National Science Foundation of China Grants No. 11072228 and No. 10772166 and the Fundamental Quality and Reliability of National Defense Science and Technology Industry of China Grant No. Z112009B004. The authors are grateful to Professor Jiming Yang and Xisheng Luo for fruitful discussions.

[1] J. W. Grove, R. Holmes, D. H. Sharp, Y. Yang, and Q. Zhang, Phys. Rev. Lett. **71**, 3473 (1993).
[2] K. O. Mikaelian, Phys. Rev. Lett. **71**, 2903 (1993).
[3] D. Hill, C. Pantano, and D. Pullin, J. Fluid Mech. **557**, 29 (2006).
[4] K. O. Mikaelian, Phys. Rev. Lett. **80**, 508 (1998).
[5] S. Gupta, S. Zhang, and N. J. Zabusky, Laser Part. Beams **21**, 443 (2003).
[6] K. Prestridge, P. Vorobieff, P. M. Rightley, and R. F. Benjamin, Phys. Rev. Lett. **84**, 4353 (2000).
[7] N. J. Zabusky and S. Zhang, Phys. Fluids **14**, 419 (2002).
[8] C. Tomkins, K. Prestridge, P. Rightley, and M. Marry-Lyon, Phys. Fluids **15**, 986 (2003).
[9] S. Kumar, P. Vorobieff, G. Orlice, A. Palekar, C. Tomkins, C.

Goodenough, M. Marry-Lyon, K. Prestridge, and R. F. Benjamin, Physica D **235**, 21 (2007).

[10] G. Layes, C. Mariani, G. Jourdan, L. Houas, F. Renaud, and D. Souffland, in *Proceedings of 10th International Workshop on the Physics of Compressible Turbulent Mixing*, edited by M. Legrand and M. Vandenboomgaerde (Paris, France, 2006).

[11] P. B. Puranik, J. G. Oakley, M. H. Anderson, and R. Bonazza, Shock Waves **13**, 413 (2004).

[12] E. Meshkov, Fluid Dyn. **4**, 101 (1972).

[13] J. S. Bai, J. H. Liu, T. Wang, L. Y. Zou, P. Li, and D. W. Tan, Phys. Rev. E **81**, 056302 (2010).

[14] P. Colella and P. R. Woodward, J. Comput. Phys. **54**, 174 (1984).

[15] W. Vreman, Phys. Fluids **16**, 3670 (2004).

[16] J. S. Bai, T. Wang, P. Li, L. Y. Zou, and D. W. Tan, Sci. China, Ser. G **39**, 1646 (2009).

[17] C. A. Zoldi, Ph.D. thesis, State University of New York at Stony Brook, 2002.